



Large eddy simulation of a dual-mode scramjet with direct injection: Flame dynamics under flow separation induced by heat-release

Mengcheng Yuan^a, Ping Wang^{a,*}, Yang Zhang^a, Ye Tian^b, Shuang Chen^b, Subhajit Roy^a, Kang Cheng^a

^a Institute for Energy Research, Jiangsu University, Zhenjiang, 212013, China

^b Science and Technology on Scramjet Laboratory, China Aerodynamics Research and Development Center, Mianyang, 621000, China

ARTICLE INFO

Article history:

Received 4 July 2022

Received in revised form 21 March 2023

Accepted 11 May 2023

Available online 18 May 2023

Communicated by Bing Wang

Keywords:

Supersonic combustion

Dual-mode scramjet

Large-eddy simulation

Flame dynamics

Flow separation

ABSTRACT

The combustion process in the scramjet engines generally takes place in unsteady conditions. The unsteadiness of the flame can be present locally or globally in supersonic combustion, for instance, reactant mixing, ignition, flame stabilization, and blow-off. Thus, unsteady supersonic combustion is an urgent problem that needs to be solved for real scramjet engine applications. This work helps to advance the knowledge of dual-mode scramjet combustion operating with different equivalence ratios by conducting quantitative analyses that characterize flame dynamics under flow separation. A hydrogen-fueled direct-injection scheme was computed using *blastFoam* code via large-eddy simulation of a scramjet test rig at a stagnation temperature of 950 K and a pressure of 0.82 MPa. The computational results were in good agreement with the experimental data, and two typical flame structures (cavity shear-layer and cavity assisted jet-wake stabilized flame) corresponding to the scram/ram operating modes were reproduced. The local flame structure and flow regime were investigated using a modified flame index and filter functions. A particular focus was set on the continuous flame flashback during mode transition, which could be divided into three stages involving jet/shear-layer interaction, unsteady heat release, and the establishment of a large-area separation zone, with the decay of the cavity recirculation zone. Additionally, the unsteady jet-wake ram combustion presented three oscillation modes, giving rise to intermittent flameout of varying levels. The coherent-structures motion caused by the combined effects of low-speed separated flow and the fuel-jet was the main cause for this kind of unsteady combustion.

© 2023 Elsevier Masson SAS. All rights reserved.

1. Introduction

The national research on near-space vehicles has been regularly boosted to achieve higher flying speed and longer strike range as a result of the growing attention devoted to the strategic potential of near-space systems [1]. Given its higher speed, lower weight, and longer range, the Dual-Mode Scramjet (DMSJ) engine has been viewed in this context as a leading candidate to accomplish the objective. A scramjet engine synergistically designed to operate as a scramjet or ramjet has no physical throat between the combustor and expansion system, thus providing an optimum cycle over a wider Mach number regime ($Ma_f = 3 \sim 8$) [2]. When the flight Mach number $Ma_f = 3 \sim 6$, the airflow entering the combustor is subsonic, i.e., ram mode. The supersonic flow predominates in the combustor to avoid excessive energy loss when the flight Mach

number is greater than 6, i.e., scram mode. Owing to the distinctive inflow conditions, the operational performance of a scramjet is basically determined by the flame-holder design through its influence on the fluid dynamics and combustion stability. In the history of scramjet engines, the combustor consisting of cavity and rear-wall expansion has emerged as a preferred configuration due to its low thrust loss and minimal aerodynamic heating [3]. As it stands, the demand for accurate flow field reproduction of realistic engine operating conditions in a corresponding configuration is increasing rapidly.

A fixed-geometry DMSJ engine's mode transition control is often achieved by altering the fuel injection regularity [4]. Tian et al. [5] experimentally studied the combustion mode in a hydrogen-fueled direct-injection scramjet and found that the transition threshold equivalence ratio (*ER*) was 0.23 under Mach 4 flight conditions. Zhang et al. [6] investigated the transition process via an experiment with a continuous increase in equivalence ratio, and concluded that the large equivalence ratio slope would not lead to

* Corresponding author.

E-mail address: pingwang@ujs.edu.cn (P. Wang).

slope variation of pressure rising even at high Mach numbers. The mode transition process in a strut-based combustor with a combined injection strategy was numerically explored by Huang et al. [7], and it was reported that the airflow conditions and the jet to crossflow pressure ratio both had a large impact except the injection strategy. By varying the injection pressure, Yan et al. [8] compared the transition processes from scram to ram and from ram to scram. The results revealed that the transition from ram to scram was more challenging than from scram to ram, and the shock waves were still in the isolator when the combustor entered scram mode. Also, a lot of effort has been put into studying the mechanisms that stabilize combustion [5,9–11]. Three common stabilization modes may be distinguished [9] based on where the flame anchors: cavity shear-layer stabilized combustion, cavity assisted jet-wake stabilized combustion, and combined cavity shear-layer/recirculation stabilized combustion. The correlation between operating and stabilization modes of the DMSJ combustor was further investigated by Yuan et al. [10], who observed that the flame was stabilized in the cavity shear-layer at scram mode while in the jet-wake at ram mode.

Although a significant amount of research has been done on scramjet investigations using a variety of configurations and injection schemes [12–14], most publications currently in print concentrate on the quasi-steady state that represents stable flame, while limited research is available on the dynamic processes that represent unstable flame, such as ignition dynamics [15], thermal-acoustic oscillation [16], flame flashback [17], and flow-induced unstable flame [18]. Therein, the flow instabilities may be attributed to the self-sustained cavity shear-layer oscillation [19], unsteady jets in supersonic crossflow [20], and separated boundary layers [21]. Wang et al. [19] have numerically found two flow-related combustion oscillation mechanisms in the scramjet with hydrogen injected upstream of the cavity. One was the intermittent auto-ignition of mixture packets linked to the fuel jet, and the other was the unsteady flame propagation affected by the jet/cavity shear-layer interaction. In the simulation of a cavity-floor direct-injection scramjet, Sitaraman et al. [22] also noticed low-frequency heat release and pressure oscillations and attributed them to the periodic fluctuation of jet penetration brought on by the interaction with the shear layer. In a DMSJ engine, intensive heat release will alter the inflow conditions through the large-scale flow separation induced by upstream-propagating back-pressure, which in turn modulates the flame stability downstream [23]. The possible interaction with fuel jets complicates the instability process even more. According to a series of well-known studies [5,9,24,25], once the heat release reached a high enough level, there was a noticeable unsteadiness. Wang et al. [26] experimentally studied the oscillation features of shock-train structures in an isolator with a choked throat, and found that the shock-train oscillation could propagate further downstream along the thicker boundary layer, resulting in drastic coherence and pressure fluctuations in downstream separated flow. Fotia et al. [18] carried out an experimental study on the hydrogen-fueled DMSJ engine and observed some low-frequency periodic oscillations of the flame position under the separated flow, which could be correlated with the upstream unsteady pre-combustion shock-train.

Combustion mode transition is usually accompanied by the transient establishment of flow separation. The combustion instabilities associated with mode transition are typically more intense and severe due to the tendency toward cavity flame blowout [21]. Yang et al. [27] provided a mechanical model of the DMSJ engine to analyze the mode transition mechanisms. It was found that the mode transition was a nonlinear and unstable process with significant Mach number fluctuations that had an adverse effect on the scramjet's stability. Kato et al. [28] conducted an experimental investigation on the flame behavior during scram to ram transition.

They have concluded that the flame fluctuated in the isolator due to the coupling between fluid dynamics and combustion and that the reversely propagating deflagration flame occurred when the thermal choke was established. In a DMSJ engine with fin-guided injection upstream of the cavity, the scram-to-ram transition was experimentally studied by Aguilera et al. [29]. The findings indicated that the transition process could be characterized by a series of flame oscillations driven by hopping cycles, which included transient thermal choking, flame flashback, cavity flame-holding, and detachment. The combustion flow field in a scramjet is inherently unstable and is characterized by the presence of temporal oscillations that have an impact on the fluid flow, mixing, and heat release. Although separation-driven supersonic combustion instability has not yet received enough attention [30], research on backpressure-induced unstable flames is very important in order to understand their physical mechanisms and impose appropriate controls.

Large-eddy simulation (LES) shows a high potential to predict such time varying phenomena [17,22,31,32]. Given these justifications, the present work uses *blastFoam* [33], an open-source generally/highly compressible reactive system solver, to perform LES for two operating conditions illustrative of dual-mode scram/ram combustion in a configuration identical to the experiment of Tian et al. [5]. The primary objective is to obtain a comprehensive understanding of flow characteristics, flame stabilization mechanisms, and unsteady flame dynamics in separated flow. The paper is structured as follows: The next section describes the methodology and quantitative comparison. After that a phenomenological description of flame stabilization mechanism is presented following a comprehensive analysis of the optical and numerical images. Then, the combustion and flow regimes are vividly demonstrated. Subsequently, the temporal evolution of dynamic behaviors, including mode transition and oscillating flame, is characterized to reveal the potential control mechanism. Finally, some significant conclusions are drawn.

2. Formulation and methodology

2.1. Numerical approach

2.1.1. Governing equations

The simulations are performed using the density-based, multi-species, reactive solver *blastFoam* that is built against the OpenFOAM C++ library. Either a local grid-size ($\bar{\Delta}$) based spatial filter (denoted with superscript “ $-$ ”) or a Favre filter (denoted with superscript “ \sim ”) is used to derive the LES governing equations from the reactive Navier–Stokes equations, which are given as follows

$$\frac{\partial \bar{\rho}}{\partial t} + \frac{\partial \bar{\rho} \tilde{u}_j}{\partial x_j} = 0 \quad (1)$$

$$\frac{\partial \bar{\rho} \tilde{u}_j}{\partial t} + \frac{\partial}{\partial x_j} (\bar{\rho} \tilde{u}_i \tilde{u}_j + \bar{p} \delta_{ij}) = \frac{\partial}{\partial x_j} (\bar{\tau}_{ij} - \bar{\tau}_{ij}^{sgs}) \quad (2)$$

$$\begin{aligned} \frac{\partial \bar{\rho} \tilde{E}}{\partial t} + \frac{\partial \tilde{u}_j}{\partial x_j} (\bar{\rho} \tilde{E} + \bar{p}) &= \frac{\partial}{\partial x_j} \left[\tilde{u}_i \bar{\tau}_{ij} + \bar{\alpha} \frac{\partial \tilde{h}_s}{\partial x_j} + H_j^{sgs} \right] \\ &+ \sum_{k=1}^{Ns} (\bar{\omega}_k \cdot h_k) \end{aligned} \quad (3)$$

$$\frac{\partial \bar{\rho} \tilde{Y}_k}{\partial t} + \frac{\partial \bar{\rho} \tilde{u}_j \tilde{Y}_k}{\partial x_j} = \frac{\partial}{\partial x_j} \left[D_k \frac{\partial \tilde{Y}_k}{\partial x_j} + \Gamma_{j,k}^{sgs} \right] + \bar{\omega}_k \quad (4)$$

here ρ , u_j and τ_{ij} are the density, velocity components and viscous stress tensor, respectively. The terms denoted with the superscript “*sgs*” are unresolved and must be modeled. The total

energy is represented by $E = h_s - p/\rho + u_j^2/2$ where h_s is the sensible enthalpy. The thermal diffusivity is given by $\alpha = \lambda/c_p$ and the thermal conductivity λ is calculated by the Eucken's approximate formula, $\lambda = \mu c_v (1.32 + 1.77R/c_v)$. Whereas, Y_k , h_k , D_k and $\dot{\omega}_k$ represent the mass fraction, static enthalpy, mass diffusivity and reaction rate of species k , respectively. The mass diffusivity is often characterized in terms of the molecular Schmidt number $D_k = \mu/Sc_k$ and $Sc_k = 0.7$ for all the species. The molecular dynamic viscosity μ is estimated using the Sutherland's law of viscosity. The static pressure p is calculated using the ideal gas equation of state, $p = \rho R_u T \sum_{k=1}^{Ns} Y_k/M_k$ where R_u , T and M_k are the universal gas constant, static temperature and species molecular weight, respectively. The thermodynamic parameters c_p , c_v , h_s are computed based on the JANAF polynomials [34].

2.1.2. Subgrid-scale modeling

Yoshizawa et al. [35] proposed an one-equation eddy-viscosity model by articulating the transportation process of SGS turbulence kinetic energy k_{sgs} in order to close the unresolved terms generated from the filtering process

$$\frac{\partial k_{sgs}}{\partial t} + \frac{\partial \bar{u}_j k_{sgs}}{\partial x_j} = -\tau_{ij}^{sgs} \frac{\partial \tilde{u}_j}{\partial x_i} - C_\varepsilon \frac{k_{sgs}^{3/2}}{\Delta} + \frac{\partial}{\partial x_j} \left[\nu_t \frac{\partial k_{sgs}}{\partial x_j} \right] \quad (5)$$

here, the terms on the right-hand side of the above equation represent production, dissipation, and diffusion of k_{sgs} , respectively. The SGS stress tensor and the turbulence kinematic viscosity are modeled as

$$\tau_{ij}^{sgs} = -2\nu_t \bar{S}_{ij} + \frac{2}{3} \delta_{ij} k_{sgs}, \quad \nu_t = C_k k_{sgs}^{1/2} \bar{\Delta} \quad (6)$$

In this work, the coefficients C_ε and C_k in Eqs. (5) and (6) are determined using the relationship between SGS stresses from two times of different-scale filtering using a box filter. According to the analyses of Kim et al. [36], it is possible to cope with energy backscatter to fit the local structures of actual turbulence and correct asymptotic behavior close to the stationary walls by dynamically choosing the model coefficients from the local properties of solvable scales.

The turbulent scalar fluxes H_j^{sgs} and $\Upsilon_{j,k}^{sgs}$ are important unclosed terms in the filtered LES equations. In general, these terms are modeled using the gradient transport hypothesis

$$H_j^{sgs} = \frac{\bar{\rho} \nu_t}{Pr_t} \frac{\partial \tilde{h}_s}{\partial x_j}, \quad \Upsilon_{j,k}^{sgs} = \frac{\bar{\rho} \nu_t}{Sc_{k,t}} \frac{\partial \tilde{Y}_k}{\partial x_j} \quad (7)$$

where the turbulent Prandtl number Pr_t and Schmidt number $Sc_{k,t}$ are set to 0.9 and 0.75, respectively.

The filtered reaction rate $\dot{\omega}_k$ is modeled using the Partially Stirred Reactor (PaSR) model [37] to couple the combustion with turbulent fluctuation. This model treats each grid cell as having two parts: the fine structure, which is dominated by chemical reaction, and the surrounding one, which is dominated by turbulent mixing. As a result, the nonlinear reaction rate can be estimated by weighting the laminar finite-rate chemistry with the volume fraction of fine structure

$$\overline{\dot{\omega}_k(\rho, Y_k, T)} = \kappa \cdot \dot{\omega}_k(\bar{\rho}, \tilde{Y}_k, \tilde{T}) \quad (8)$$

where the laminar reaction rate $\dot{\omega}_k$ is calculated using filtered quantities based on the Arrhenius formula. Marinov's intricate hydrogen-air reaction mechanism [38] with 9 species and 27 elementary reactions is adopted here in order to reproduce the practical chemical kinetics of the dynamic combustion process. This mechanism has been justified in previous publications for supersonic combustion [39,40]. The volume fraction of fine structure κ

can be defined as a function of chemical time-scale τ_c and SGS mixing time-scale τ_m , i.e. $\kappa = \tau_c / (\tau_c + \tau_m)$.

In OpenFOAM, the chemical time-scale of multi-step reaction is integrated by [41]

$$\tau_c = \sum_{r=1}^{Nr} \frac{Nr \cdot c_{tot}}{\sum_{s=1}^{Ns,RHS} \nu_{s,r} \tilde{K}_{f,r}} \quad (9)$$

where c_{tot} is the total molar concentration. $\nu_{s,r}$ and $K_{f,r}$ are the stoichiometric coefficient and forward reaction rate of reaction r , respectively. Since the subgrid scale and the Kolmogorov scale are of the same order, the time scale of SGS turbulent mixing can be calculated as

$$\tau_m = C_{mix} \sqrt{\frac{\mu + \mu_t}{\bar{\rho} \bar{\epsilon}}} \quad (10)$$

here $C_{mix} = \sqrt{1/(1 + C_\mu Re_t)}$ and $C_\mu = 0.09$ in the present work. This leads to $C_{mix} \approx 0.01$, which is the typical value of turbulent flow in a supersonic channel.

2.1.3. Solving implementation

BlastFoam employs the finite-volume method along with a cell-center data storage structure for the discrete solution of computational domain. The time advancement of the evolution equations is achieved using the third order explicit strong stability-preserving Runge-Kutta method [42]. The second order MUSCL reconstruction and the VanLeer limiter are combined to interpolate the left and right states at the interface. The approximate solution of the HLLC-P Riemann solver [43], which eliminates the distortion and instability issues from the traditional HLLC scheme in the low Mach number region and is appropriate for a range of conditions from hypersonic compressible to low-speed incompressible flow regimes, is used to calculate the conservative hyperbolic fluxes. Besides that, the diffusive fluxes are discretized using the second order central differencing method.

The resulting algebraic equations are solved using the PBiCGStab method which is preconditioned by the DILU technique. Moreover, the Rosenbrock stiff ODE (Ordinary Differential Equation) solver [44] is used to integrate the overall reaction rate. The maximum Courant number is kept at 0.6 in the current computation, which corresponds to a physical time-step size of the order of 8×10^{-9} s. The residual criterion for convergence in each time-step is set to 1×10^{-12} .

2.2. Experimental and computational setup

2.2.1. Configuration description

A laboratory-scale direct-connect scramjet facility with a cavity flame-holder is being designed at China Aerodynamics Research and Development Center (CARDC) to simulate at flight Mach number $4 \sim 7$ conditions. The high-enthalpy vitiated air, which has a mole fraction of 21% O₂, 12% H₂O and 67% N₂, is accelerated to Mach 2 at the isolator entry under stagnation conditions of $p_0 = 0.82$ MPa and $T_0 = 950$ K, which correspond to a Mach 4 flight condition. At Mach 1, the hydrogen fuel is directly injected into the cavity at ambient temperature ($T_0 = 295$ K). A series of experimental studies using this facility can be found in literature [5,45,46], in which the data are collected using various measurement techniques such as schlieren, chemiluminescence photography, OH-PLIF, and differential interferometry.

The computational domain is showed by the yellow region in Fig. 1. The total length of the geometry is 400 mm, of which the isolator is composed of a 70 mm straight section and an 80 mm expansion section with a divergent angle of $\alpha = 1.4^\circ$. The height

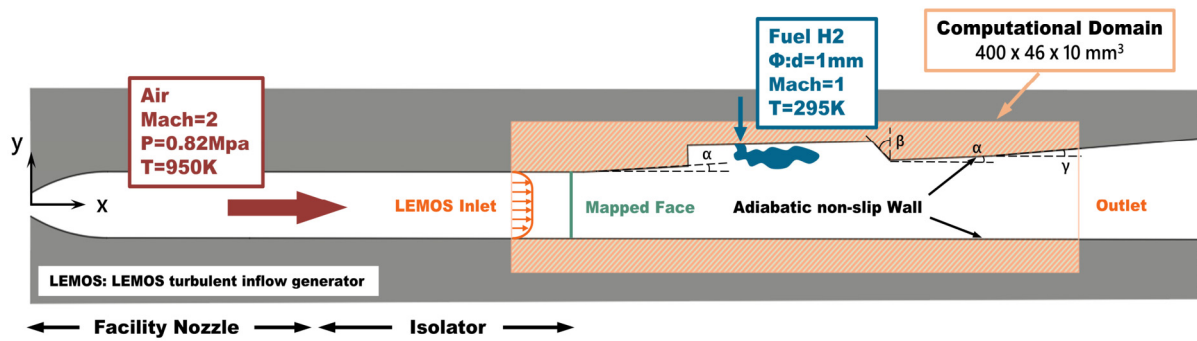


Fig. 1. Sketch of the CARDC scramjet facility. The channel surrounded by the yellow region corresponds to the computational domain. The green line is the section mapped to air inlet for the velocity profile. (For interpretation of the colors in the figure(s), the reader is referred to the web version of this article.)

Table 1
Inflow parameters for the airstream and fuel jet.

	<i>Ma</i>	<i>T_s</i> [K]	<i>p_s</i> [MPa]	<i>u</i> [m/s]	<i>Y_{H2}</i> [%]	<i>Y_{O2}</i> [%]	<i>Y_{H2O}</i> [%]	<i>Y_{N2}</i> [%]
Air	2	546	0.1	943	0	24.3	7.8	67.9
Fuel jet	1	246	0.8/2.1	1200	100	0	0	0

at the entry is 30 mm. A cavity of 121 mm in length, 11 mm in depth, is installed on the upper wall with a rear-wall-expansion angle of $\beta = 21.1^\circ$. As a result, the length and the divergent angle of expansion section's two parts are 102.5 mm, $\alpha = 1.4^\circ$ and 26.5 mm, $\gamma = 2^\circ$, respectively. Furthermore, the fuel orifices with a diameter of 1 mm are located 25 mm downstream of the cavity step. Considering the high cost of full-size computation, the present work only reserves 1/15th of the width (10 mm), containing one fuel orifice, in order to apply periodic boundary conditions in the span-wise direction (z).

2.2.2. Boundary conditions and grid

As for the inflow conditions, all the inlets are set to Dirichlet boundaries based on the experimental parameters, and the air-inlet velocity profile is mapped from the section 50 mm downstream. Additionally, synthetic turbulence with a 5% fluctuation intensity is added using the LEMOS generator [47] to reproduce the fully-developed inflow that follows a 1/7th power law. The supersonic outflow quantities are extrapolated from the nearest cells and no-slip adiabatic boundary condition is imposed on all the walls. In the current work, two cases with different global equivalence ratios (case 1: ER = 0.1 and case 2: ER = 0.3) are comparatively studied by changing the fuel jet's injection stagnation pressure ($p_0 = 1.5$ MPa and $p_0 = 4.0$ MPa), and then achieves a phenomenological scram-to-ram transition by directly switching the injection pressure from case 1 to case 2 to study the intermediate state. More inflow parameters are presented in Table 1, where the isentropic flow hypothesis is used to convert the stagnation temperature and pressure of the inflow into static values.

A multi-block structured grid which is clustered near the walls, cavity shear layer, and fuel jet is shown in Fig. 2(a). The distance between the first node and the wall is set to 0.01 mm so that the dimensionless quantity y^+ equals 10, which is a little coarse for the wall-resolved LES but appropriate for those with dynamic turbulence model [36]. The total number of grid cells is 5.0 million, with $342 \times 80 \times 38$ and $762 \times 137 \times 38$ cells inside and outside the cavity, respectively. As seen in Fig. 2(b), the volume fraction of $\tau_c / (\tau_c + \tau_m)$ for these two cases in the range approaching unity are 0.983 and 0.878, respectively. This indicates that the finite-rate chemical kinetics effect is present in almost the whole domain where $\tau_c \gg \tau_m$. Also, since the SGS turbulence has such a small impact, the grid resolution is sufficient to resolve the interaction between chemical reaction and turbulence.

2.3. Code validation

Fig. 3 compares experimental and computational pressure profiles. Here, the data are collected for 6 flow-through times ($\tau_f = L/U_\infty \approx 4 \times 10^{-4}$ s) after $5\tau_f$ in order to reach the statistical steady state. Further topologically identical coarser (1.0 million) and finer (7.0 million) grids are generated for case 1 in order to do a grid independence study. The pressure distributions on the upper wall are shown to be nearly identical apart from the leading edge of the expansion section, where the moderate and finer grids predict lower values than the coarser one, which is consistent with what was seen in Cao's investigations [11]. This might be due to local refinement capturing multiscale turbulence at the expansion fan. The simulations for both cases are conducted on the moderate grid (5.0 million) in order to make a compromise between the fidelity and efficiency. As can be seen in Fig. 3, the pressure distribution on the upper wall matches the experimental results well for both cases except the separation point pressure in the isolator for case 2, which is slightly overpredicted. The absence of good near-wall resolution might be the most important factor among the other factors explaining the overprediction. In addition, a sharp pressure drop can also be observed owing to the rapid expansion of a high-pressure jet near the inlet, but it is not captured by the discrete pressure measurements. Anyway, these discrepancies are all acceptable.

Furthermore, the Mach number distributions are verified by a 1-D pressure/Mach number response model [48] to the experimental pressure profiles

$$\frac{dT_0}{T_0} = \frac{1}{1 + (\gamma - 1) Ma^2/2} \left[\frac{\gamma Ma^2 - 1}{\gamma Ma^2} \frac{dp}{p} + \frac{dA}{A} - 4C_f \frac{1 + (\gamma - 1) Ma^2}{2} \frac{dx}{D} \right] \quad (11)$$

$$\frac{dMa}{Ma} = \frac{1}{Ma^2 - 1} \left(1 + \frac{\gamma - 1}{2} Ma^2 \right) \left[\frac{dA}{A} - \frac{1 + \gamma Ma^2}{2} \frac{dT_0}{T_0} - 4C_f \frac{Ma^2}{2} \frac{dx}{D} \right] \quad (12)$$

where $\gamma = 1.4$ is the specific heat ratio, A is the cross-sectional area of the channel, and $C_f = 0.003$ is the wall skin-friction coefficient. The hydraulic diameter D is defined as $D = 4A/d_w$ and d_w is the wetted perimeter. As shown in Fig. 4, the one-dimensional

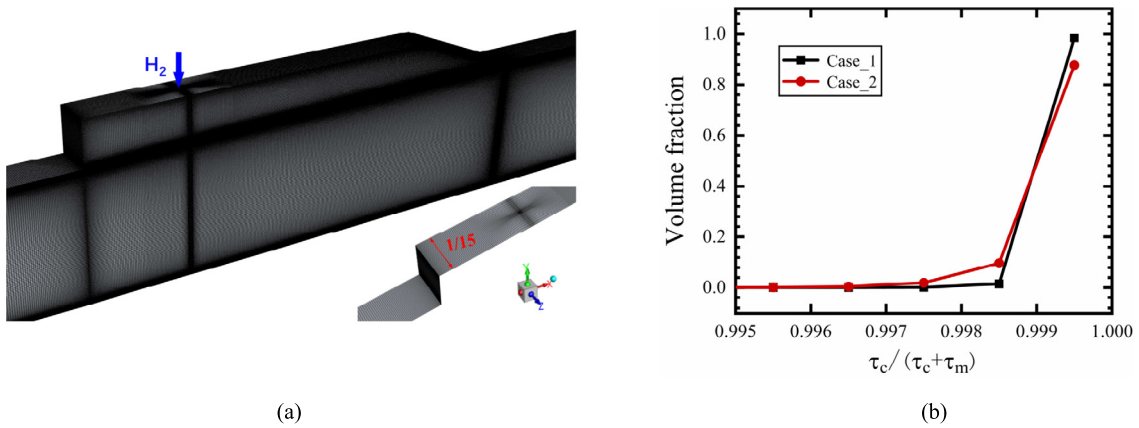


Fig. 2. (a) Computational grid for LES. (b) Volume fraction distribution of $\tau_c / (\tau_c + \tau_m)$.

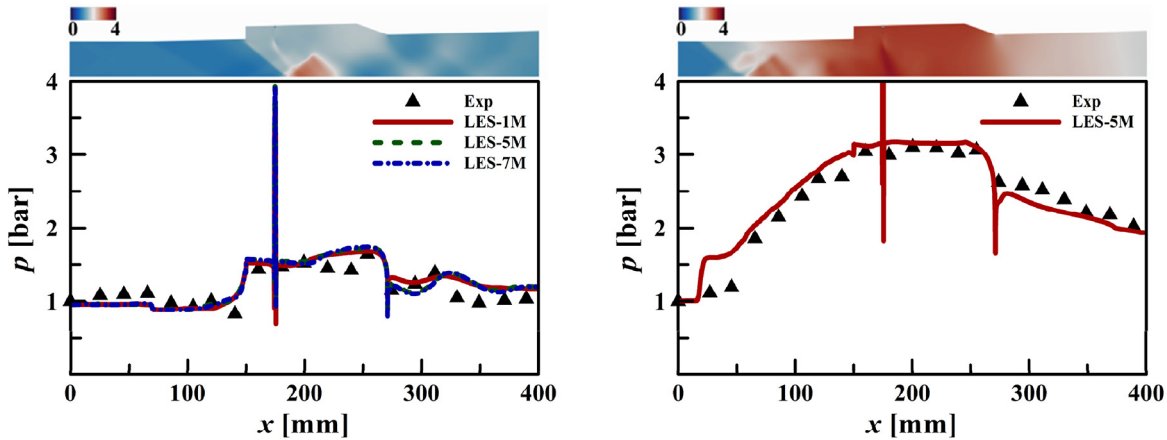


Fig. 3. Comparison of computational pressure profiles on the upper wall of case 1 (left) and case 2 (right) with Tian's experimental results [5].

Ma distributions from LES are obtained using cross-section averaging method. The extrapolated results from experimental pressure are in good agreement with the overall LES trend. For cases 1 and case 2, the cavity and isolator, respectively, contain the maximum amount of error. Without a doubt, the presence of reflected and pre-combustion shock waves in these regions, as seen in Fig. 3, causes the measured pressure on the upper wall to be lower than the cross-section averaged.

Various approaches have been proposed to identify the operating mode of the DMSJ engine, which can be broadly categorized based on the position of the significant pressure-rise point relative to the isolator exit and the size of the separation zone [49], or on the Mach number at the isolator exit [50]. In either way, it can be deduced from Fig. 3 and Fig. 4 that case 1 is in scram mode and case 2 is in ram mode.

3. Results and discussion

3.1. Quasi-steady combustion mode

The shock and shear-layer structures are depicted in Fig. 5(a). For case 1, the leading edge of the cavity serves as the source of the reflected shocks, which are then enhanced due to the obstruction of the cavity shear-layer. As a result, a high-pressure zone is produced near the bottom wall at $x = 210$ mm, as shown in Fig. 3. For case 2, the pressure in combustor rises sharply due to the intensive reaction, which propagates upstream to the isolator. Then the shock train develops from the separated boundary layer at $x = 20$ mm. The cavity shear-layer experiences severe flow oscillation as a result of the large-scale separated vortex shed at the

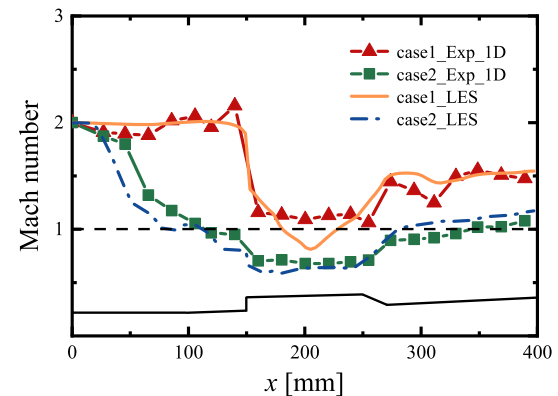


Fig. 4. Experimental and computational 1-D Mach number distributions.

step. Due to the long camera exposure time used in the experimental schlieren, the vortex evolution cannot be properly captured. However, the large-amplitude oscillation can be seen in the differential interferometry photographs, and the computational results accurately duplicate these images.

The spatial agreement of the high-temperature zone and flame structure is also achieved, as seen in Fig. 5(b) and (c). It can be found that the reaction zone of case 1 (scram mode) has a "V" shape, and most of the OH radicals are localized in the cavity shear-layer as opposed to the cavity. Moreover, the injected cold hydrogen is entrained into the corner recirculation zone, resulting in a temperature difference between the front and rear part of the cavity. In addition, a completely different flame structure can be

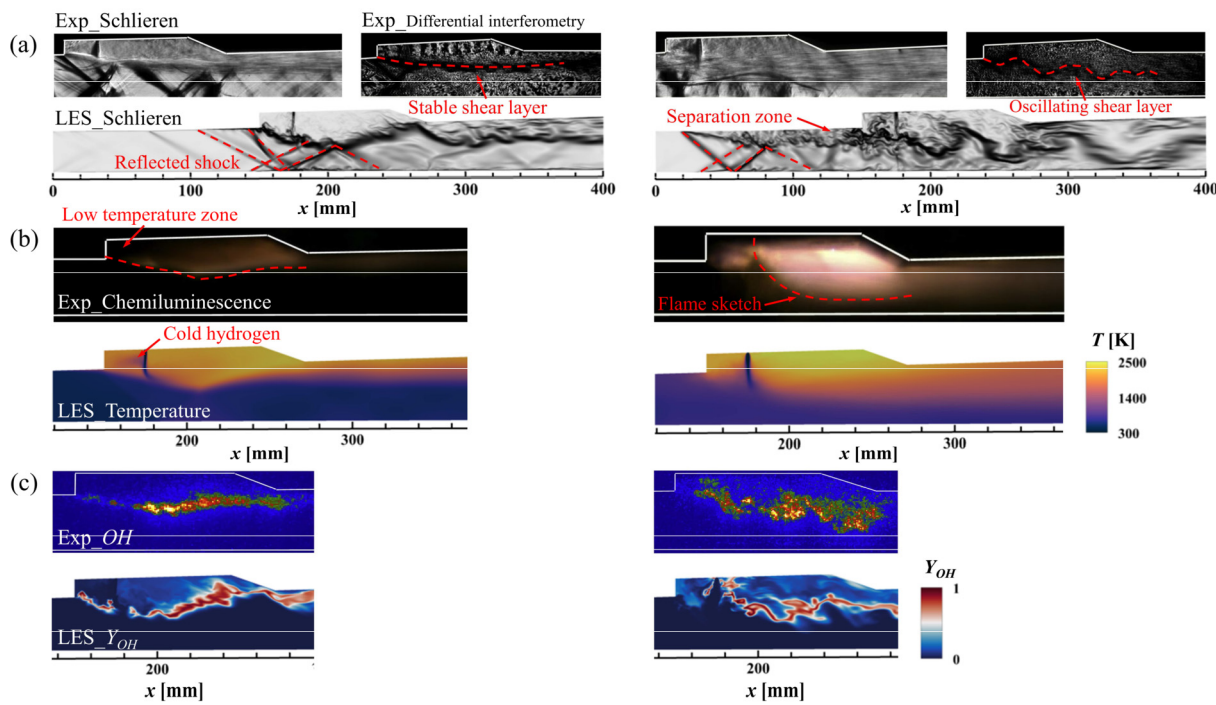


Fig. 5. Comparison of (a) instantaneous shock and shear-layer structures, (b) time-averaged temperature and chemiluminescence. (c) instantaneous normalized Y_{OH} contours of case 1 (left) and case 2 (right) in the center slice with experimental optical images [5].

observed in **case 2 (ram mode)**, which displays a parabola shape resembling a “torch”. The OH radicals spread from the fuel orifice to the downstream expansion section, with a negligible amount of them in the leading edge of the cavity. The temperature in the cavity is visibly higher than in case 1 due to the more intense heat release and the ram effect in the isolator, and the high-temperature zone is more widely distributed.

Fig. 6 shows pictures of the flow field and flame structures that have been overlapped in order to highlight the combustion stabilization mode. The fuel-jet core in case 1 has a branch due to the strong entrainment, and a significant amount of hydrogen collects in the corner to maintain the upstream flame's fuel supply. The downstream flame receives radicals and a hot environment from the cavity recirculation zone, which is located at the rear of the shear-layer. This process is known as cavity shear-layer stabilized combustion. The cold jet penetrates the shear-layer and causes local extinction, in contrast to the outcomes of injection upstream of the cavity [9]. But the whole flame remains stable, since it is mainly held by the vortex interactions with the cavity rather than the streamwise transportation. In case 2, a significant corner recirculation zone is also generated. Nevertheless, its jet momentum is higher and the recirculation velocity is lower than in case 1. In order to prevent hydrogen from being heavily entrained into the corner, hot products collect instead, acting as an ignitor. It is important to note that the cavity lacks a primary recirculation zone, which may be the result of interactions between the fuel jet and low-speed separated flow in a configuration with a large length to depth ratio ($L/D = 11$). Similarly, it can be inferred as cavity assisted jet-wake stabilized combustion, though it is susceptible to the flow oscillation.

Fig. 7 presents a comprehensive overview of two distinct combustion stabilization mechanisms in a cavity-floor direct-injection scramjet. Building upon previous studies by Yuan et al. [10], it is found that during scram mode, the fuel jet splits the cavity into two distinct regions: a rich-premixed zone and a hot product zone. The resulting flame in the cavity is discontinuous and is stabilized within the shear layers of recirculation zones. The shear layer and

fuel jet impede supersonic inflow, creating reflected shocks and a bow shock. On the other hand, during ram mode operation, the flame is stabilized in the jet-wake. Furthermore, the corner recirculation zone plays a vital role in maintaining continuous ignition of the fuel jet. Although there is no primary recirculation zone within the cavity, the hot products that flow downstream have positive effects on the jet-wake flame. This is because pure jet-wake stabilized combustion is not attainable under low inflow stagnation temperatures [9]. Additionally, the shear layer and shock train exhibit violent oscillations due to large-scale vortex shedding. As a result, the flow field is complex and intrinsically unstable.

3.2. Combustion and flow regimes

Takeno Flame Index (TFI) expressed as $TFI = (\nabla Y_F \cdot \nabla Y_O) / |\nabla Y_F \cdot \nabla Y_O|$ can be used to characterize the flame regimes, where “ $TFI = -1$ ” and “ $TFI = 1$ ” denote diffusion and premixed regimes, respectively. Additionally, the level of fuel-rich for local premixed regime can be distinguished by weighting with the mixture fraction Z . Building upon this framework, the current work proposes a Modified Flame Index (MFI) that incorporates the unit-volume heat-release rate to differentiate the flame from flow field

$$MFI = \frac{1}{2} \frac{Z - Z_{st}}{|Z - Z_{st}|} \times (1 + TFI) \times \frac{1 + \text{sign}(HRR - \bar{HRR})}{2} + \text{sign}(HRR - \bar{HRR}) - 1 \quad (13)$$

in which Z is calculated from Bilger et al. [51], and $Z_{st} = 0.0219$ at stoichiometry. $\bar{HRR} = 2 \times 10^8 \text{ W/m}^3$ is the volume-averaged heat-release rate. The flame regimes indicated by different values are: no flame ($MFI = -2$), lean-premixed flame ($MFI = -1$), diffusion flame ($MFI = 0$), and rich-premixed flame ($MFI = 1$), respectively.

Fig. 8(a) illustrates that both cases exhibit the characteristics of diffusion regime as a whole. Specifically, the rich-premixed regime is observed in the vicinity of the fuel jet, while the diffusion regime dominates the remaining region. Notably, the location of the rich-premixed regime differs between the two cases, with case

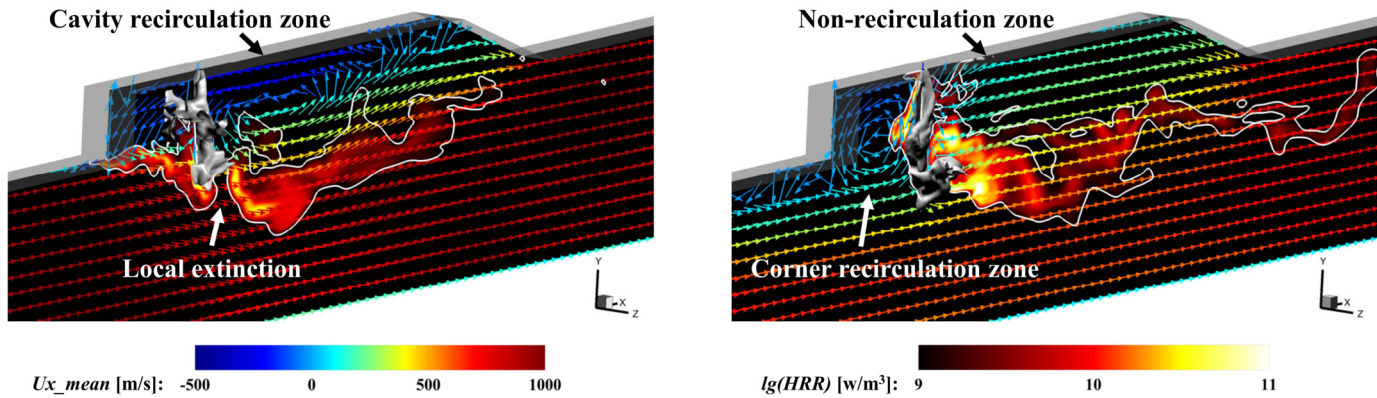


Fig. 6. Time-averaged distribution of velocity vector colored by streamwise component, overlaid with the instantaneous heat-release rate (logarithmic scale) contour and iso-surface of $Y_{H_2} = 0.1$ in case 1 (left) and case 2 (right). The white lines denote $HRR = 1.0 \times 10^9 \text{ W/m}^3$.

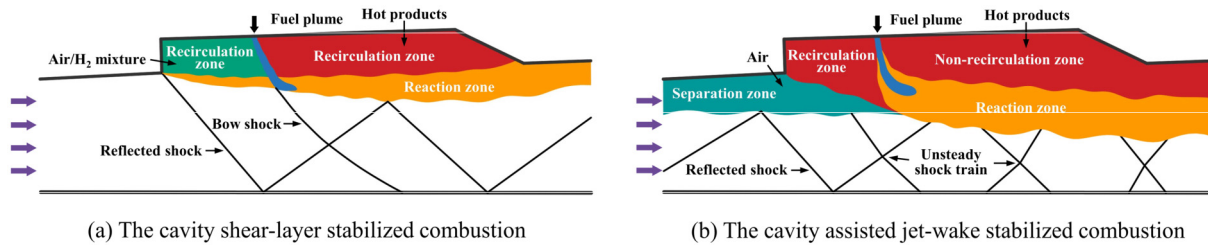


Fig. 7. Schematics of flame stabilization mechanism in the cavity-floor direct-injection scramjet.

1 displaying it on the cavity side of the shear layer and case 2 on the inflow side of the flame head. Additionally, it is interesting to observe that the lean-premixed regime occurs in a narrow layer where the flame interacts with the incoming airstream. This occurrence can be attributed to the dilution effect of the downstream-developing rich-mixture, which is entrained by the counter-rotating streamwise vortex-pairs, as previously observed in Liu's research [52].

Fig. 8(b) shows the engine's perspective views, where the vortex structures are identified using the Q-criterion iso-surface ($1 \times 10^5 \text{ s}^{-1}$). The 3-D vortex structures in the cavity of case 2 are found to be larger than those of case 1, primarily initiated by the shock/boundary-layer interaction in the isolator and intensified by thermal expansion in the cavity. Moreover, hairpin-like vortexes induced by the shock/boundary-layer interaction are observed on the lower wall. Both flames are confined in the vortexes that enhance fluid mixing, causing the flame in case 1 to be inside the cavity or close to the upper wall of the expansion section, while that in case 2 oscillates violently and the intermittent blowoff is observed downstream. Fig. 8(c) shows the time-averaged Mach number contours, embodying two typical features of a dual-mode scramjet. In scram mode, the flow in almost the entire combustor, except for the cavity, is supersonic. In ram mode, the subsonic region extends to the isolator and expansion section, and the supersonic channel is similar to the Laval nozzle, with a thermal throat at the cavity rear-part ($x = 250 \text{ mm}$).

Scrutinizing the local flow regimes is significant for comprehending the underlying mechanisms driving mode transition. Fig. 9 demonstrates the 1-D supersonic vs. subsonic and upstream vs. downstream mass flow ratio ($\dot{q}_{m,\text{local}}/\dot{q}_{m,\text{tot}}$) along the engine length. Notably, since the flow in recirculation zones is primarily subsonic, the supersonic upstream regime is excluded from the analysis. Inspired by the work of Cao et al. [11], the filter functions used to extract the local mass flow rate of mixture through a cross section are defined as

$$\dot{q}_{m,\text{sup}} = \int \frac{1 + \text{sign}(Ma - 1)}{2} \rho u_x dA \quad (14)$$

$$\begin{cases} \dot{q}_{m,\text{sub1}} = \int \frac{1 + \text{sign}(1-Ma)}{2} \cdot \frac{1 + \text{sign}(u_x)}{2} \rho u_x dA \\ \dot{q}_{m,\text{sub2}} = \int \frac{1 + \text{sign}(1-Ma)}{2} \cdot \frac{1 - \text{sign}(u_x)}{2} \rho u_x dA \end{cases} \quad (15)$$

where the subscripts "sub1" and "sub2" in Eq. (15) denote the subsonic downstream and upstream regimes, respectively. In scram mode (case 1), the supersonic downstream flow consistently comprises more than 90%. The subsonic downstream flow reaches its peak (10%) at $x = 190 \text{ mm}$, which is slightly upstream of the location with the minimum Mach number ($x = 200 \text{ mm}$) depicted in Fig. 4. And the subsonic upstream flow attains its peak (1.6%) precisely at $x = 200 \text{ mm}$, thereby indicating the location of the cavity-recirculation core. In ram mode (case 2), the ratios of supersonic and subsonic downstream flow are almost symmetrical. One may observe that their ratios are equal at $x = 175 \text{ mm}$, with each accounting for 50%. After that, the supersonic downstream flow ratio experiences a brief rise before declining to its minimum value (43%) at the thermal throat. Furthermore, there exist two peaks of subsonic upstream flow ratio within the engine, which occur at $x = 75 \text{ mm}$ in the isolator and at $x = 160 \text{ mm}$ in the cavity corner. The recirculation ratio in the corner recirculation zone (1.5%) is lower than that in the separation zone (2%), although it is higher than that in case 1 at the same location.

3.3. Scram-to-ram transition

This section examines the dynamic behaviors of shock wave and flame during scram-to-ram transition, both qualitatively and quantitatively. Fig. 10 presents the evolution of pressure and flame during the mode transition. In the left-hand figures, the white arrows indicate the direction of oblique shocks propagation. Following an increase in injection pressure, a high-pressure zone is generated below the jet due to the impeding effect with the forward propagating shocks. At snapshot "C", the shocks are blown back into the cavity owing to pressure relief and insufficient heat-release, and a normal shock is observed in the cavity entrance, as

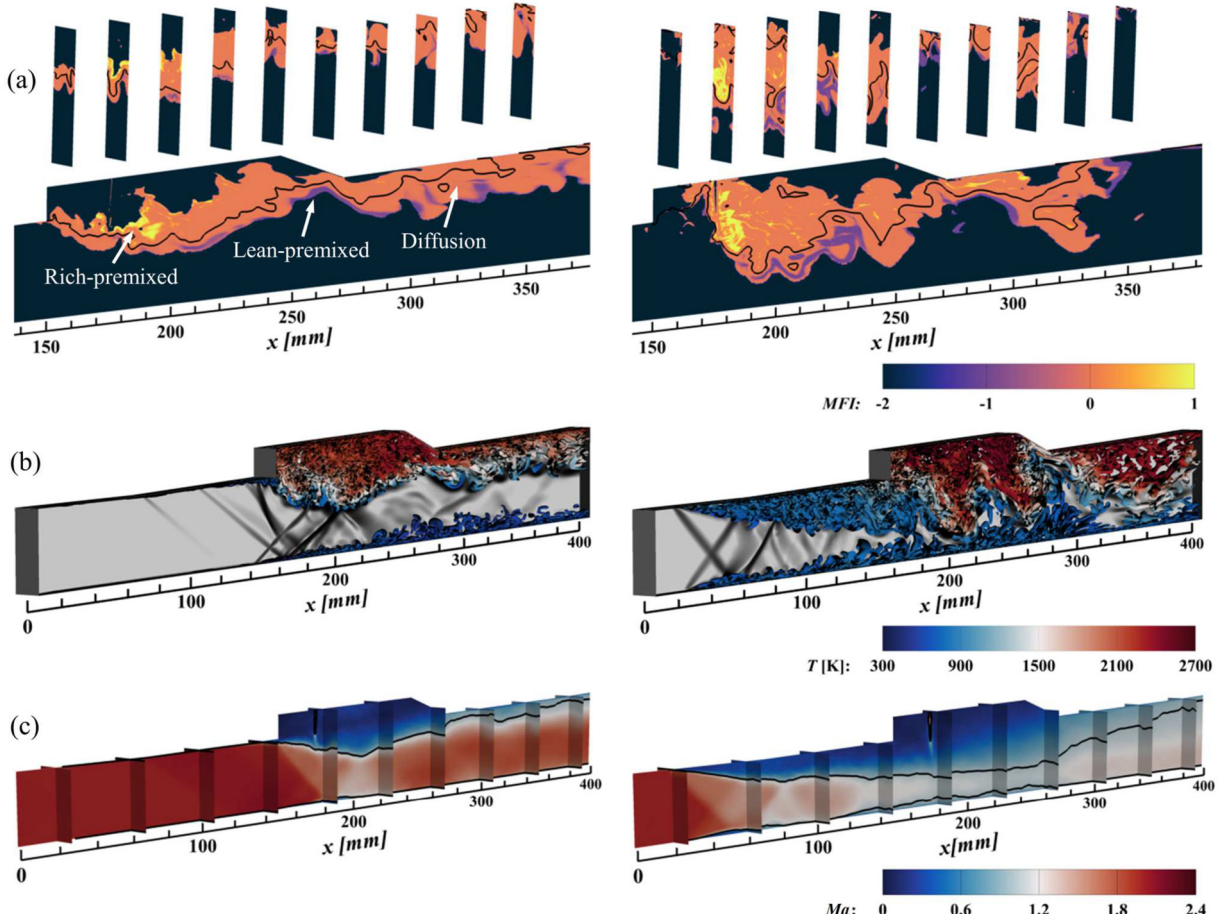


Fig. 8. Contours of (a) instantaneous modified flame index MFI with black isoline at stoichiometry, (b) instantaneous shock and vortex structures colored by temperature, and (c) time-averaged Mach number with black isoline at sonic speed of case 1 (left) and case 2 (right).

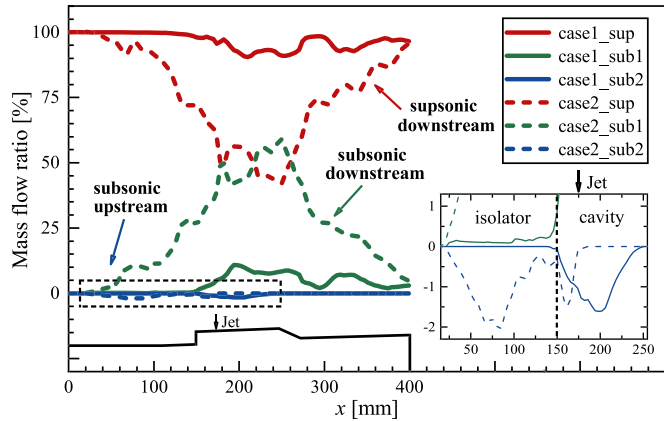


Fig. 9. Time-averaged mass flow ratio of combined speed and direction.

indicated by the dotted circles. Similarly, the reciprocating process is observed again from snapshots "D" to "E", but the shock waves can now reach farther upstream, and the pressure in combustor is higher due to further heat-release. At snapshot "F", the oblique shocks oscillate slightly near the isolator entrance when incoming air is in dynamic balance with the pressure in combustor.

In the first three snapshots on the right of Fig. 10, the sudden increase of injection pressure causes violent shear-layer oscillation, and the flame tail keeps switching between attachment and detachment from the cavity tailing edge. The dotted circles show the appearance of flame flashback in the early stage. Although the

flame is highly wrinkled, it is still stabilized by the cavity. Snapshot "D" can be inferred to be at the unsteady transitional mode, where the jet-wake flame gradually forms. The flame leading edge is distorted by separated flow, and flame flashback occurs. Nevertheless, it is still possible for the flame to return to cavity mode. This oscillation phenomenon between two combustion modes is also reported in Nakaya's studies [20], which indicate that the vortices generated by the separated boundary layer induce a strong jet-wake flame, resulting in the transient thermal choking followed by shear-layer stabilized ram combustion. In snapshots "E" and "F", the flame leading edge is entrained into the corner recirculation zone, which is hard to maintain stable combustion under such a strong disturbance. Therefore, the combustor is at the jet-wake mode in this stage.

Fig. 11 depicts the developmental process of the low-energy stream. Examining the recirculation zone of the cavity in the left-hand figures reveals that the low-speed separated flow is inadequate to establish recirculation downstream of the jet as the separation zone advances. The first three snapshots exhibit an evident recirculation, which corroborates the aforementioned cavity stabilized mode. When combined with the flame structure shown in Fig. 10, it is apparent that the jet-wake stabilized mode is established when the cavity recirculation zone completely disappears. Furthermore, when observing the pressure evolution, it is found that the boundary layer separates from the wall due to the adverse pressure gradient when shock waves propagate upstream, and return to attach to the wall when normal shock is generated at the separation point upon downstream propagation.

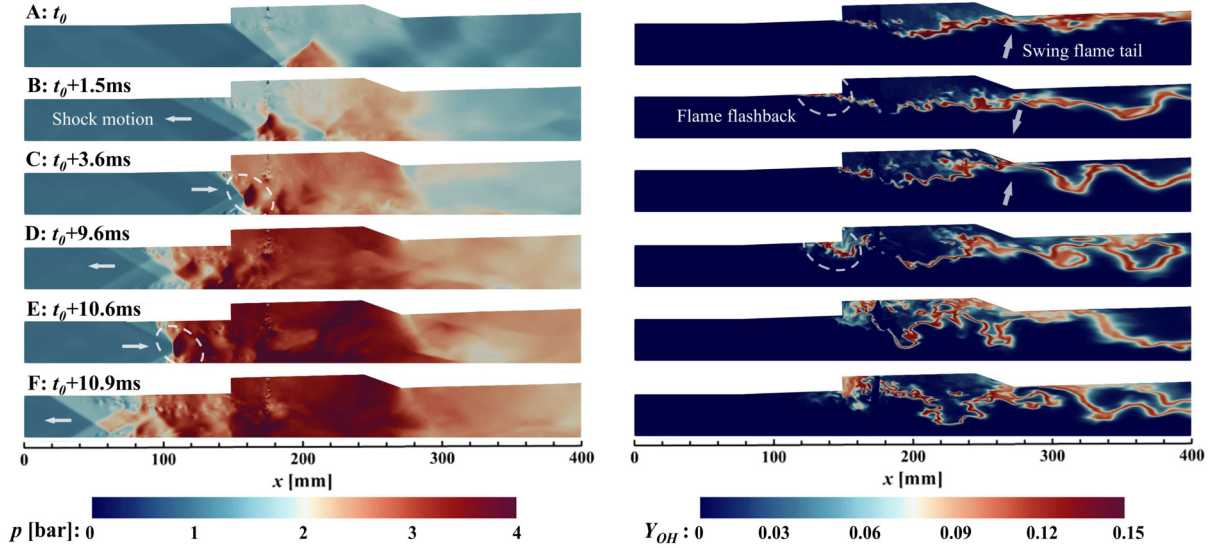


Fig. 10. Instantaneous snapshots of pressure (left) and Y_{OH} (right) in the center slice during mode transition.

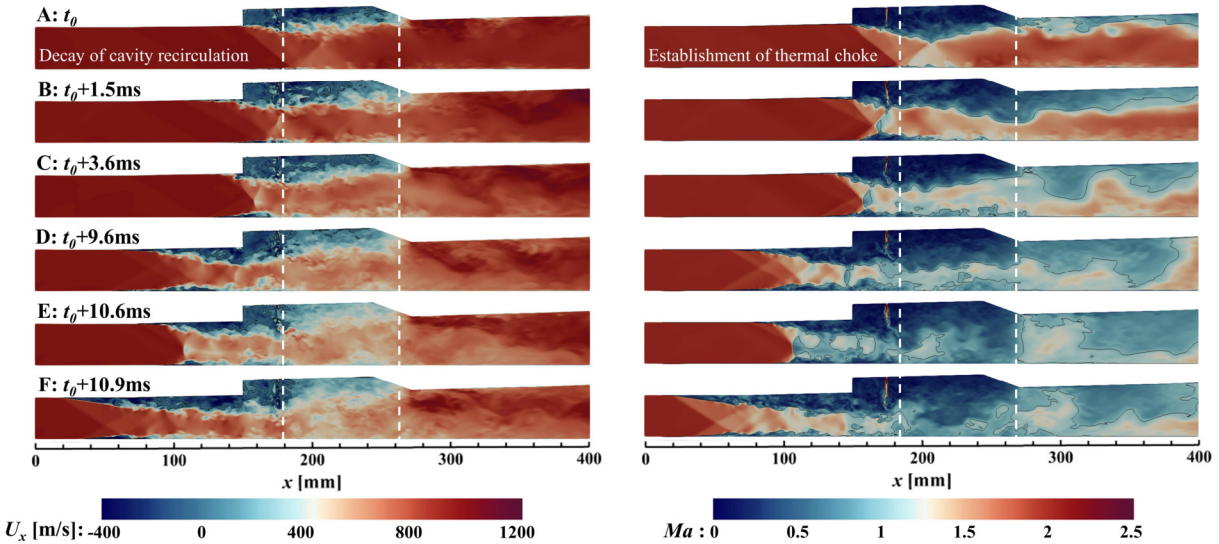


Fig. 11. Instantaneous snapshots of streamwise velocity (left) with black isoline at $u_x = 0$ m/s, and Mach number (right) with black isoline at sonic speed, in the center slice during mode transition.

The Mach number evolution depicted in Fig. 11 indicates that the distribution of the subsonic region has a direct impact on the flame movement range. In the first three snapshots featuring the swing flame, the subsonic region at the tailing edge of the cavity periodically becomes larger and smaller. From snapshots "D" to "F", thermal choking gradually strengthens as the flame oscillates near the lower wall. Additionally, the thermal throat is located at the rear part of the cavity, indicating that the jet-wake flame dominates in heat release.

Fig. 12 presents the temporal evolutions of pressure signals and flame flashback distance. Notably, the pressure waveform measured in the cavity (P1) exhibits a high-frequency oscillation, which can be attributed to the acoustic motion in the subsonic region [22]. Additionally, the pressure response recorded in the tail of the isolator (P2) depicts the upstream propagation of backpressure. Based on the severity of the flame flashback, the entire process can be categorized into three stages. In stage #1, the pressure in the cavity rapidly increases with an increase in injection pressure. Although a weak backpressure is observed in the isolator, a severe flashback phenomenon is observed, which is also evident in the

early stage of Fig. 10. This phenomenon is mainly associated with the sudden disturbance of the jet to shear-layer under stronger penetrability. In stage #2, the pressure tendency in the cavity remains relatively stable, and the combustor is in a state of energy accumulation by heat-release. The propagation abilities of back-pressure and flame flashback are both weak, while the frequency is notably higher due to unsteady heat-release. In the critical stage of mode transition (stage #3), long-term and large-amplitude pressure responses can be detected in the isolator, indicating the establishment of a large-area separation zone. Furthermore, multiple reciprocating oscillations of the separated flow and continuous severe flame flashback phenomenon can be observed. The obvious large-amplitude oscillation mode with a rapid-growing trend is monitored in the cavity, which is caused by the continuous pressurization and depressurization cycles. It can be inferred that the transient thermal choking occurs in this stage, and the intensive heat-release plays a significant role in promoting the mode transition in this stage.

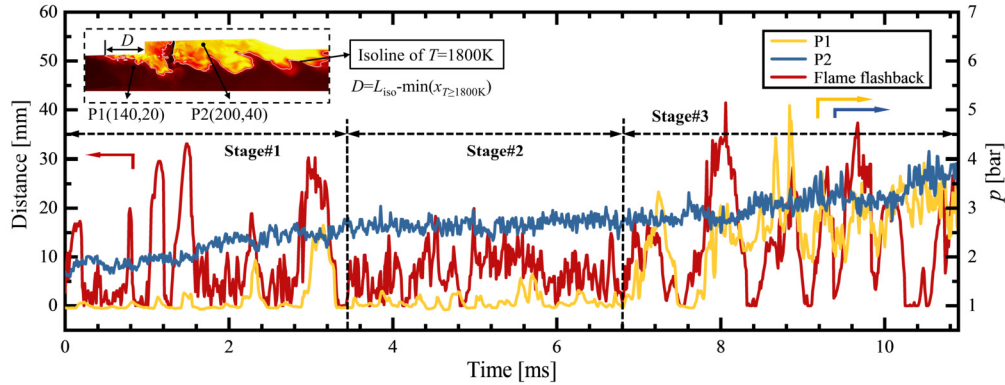


Fig. 12. Temporal histories of pressure signal and flame flashback distance oscillations.

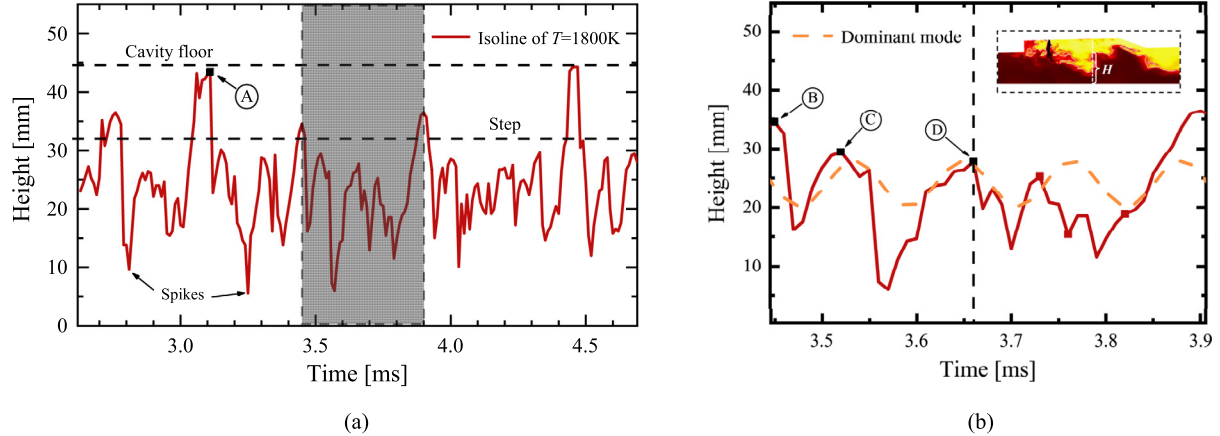


Fig. 13. (a) The waveform of flame oscillation in case 2. (b) The view zooming in grey region.

3.4. Flame behavior under separated flow

Under the current conditions, a stable primary recirculation zone cannot be generated in the cavity during ram mode operation. Consequently, the flame is highly susceptible to the combined effects of large-scale separation vortices and fuel jet. Even when subjected to severe shear-layer oscillations, the flame is prone to intermittent flameout [9]. In order to examine the impact of coherent structures on flame behavior under the combined action of unstable inflow and vertical jet. This work utilizes the height variation of the $T = 1800\text{ K}$ isoline at $x = 220\text{ mm}$ in the center slice to characterize the flame oscillation level, as shown in Fig. 13. The temporal evolution of the flame covers a maximum oscillation period (mode #3) from $t = 3.05\text{ ms}$ to $t = 4.45\text{ ms}$, during which the flame exhibits the largest amplitude and almost touches the cavity floor. In mode #2 ($t = 3.45 \sim 3.90\text{ ms}$), the flame position extends beyond the cavity step but does not reach the floor. Fig. 2 provides a close-up view of mode #2, with the yellow line denoting the dominant mode (mode #1) and a frequency of approximately 8796 Hz. It is evident that the dominant mode corresponds to the self-sustained shear-layer oscillation induced by vortex shedding.

Fig. 14 presents a series of crucial flame snapshots that correspond to the phases displayed in Fig. 13. At snapshot "A", the shedding vortex collides with the rear-wall of the cavity, causing a considerable amount of the "free-stream" fluid to be entrained by the vortex and transported into the cavity. Furthermore, the flame becomes so severely wrinkled that it nearly detaches downstream. Snapshots "B" to "D" depict the sequential motion of the vortices in mode #2, where the flame oscillates at the cavity step height. The periodic law of jet penetration depth variation, accompanied by vortex shedding, can be determined. The high-momentum jet

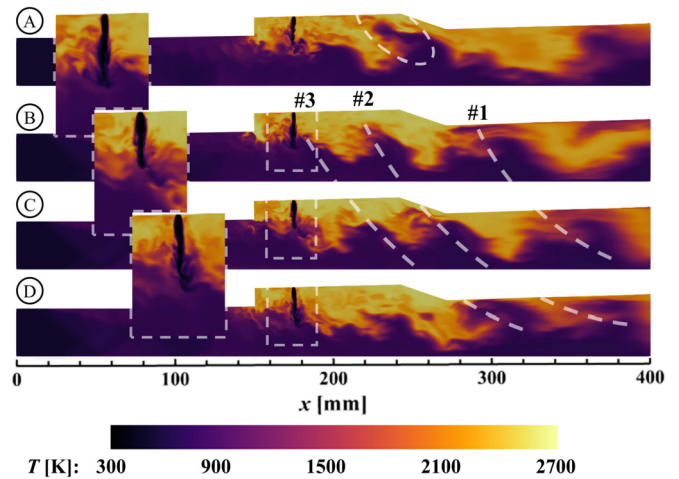


Fig. 14. The key snapshots of flame evolution with zooming in fuel jet.

can either promote or inhibit vortex shedding, which subsequently disintegrates the fuel jet. As demonstrated in snapshot "C", once the fuel jet collides with the shedding vortex at the cavity step, it commences disintegrating, resulting in a reduction in penetration depth. Additionally, it is noteworthy that the interval between vortex #1 and vortex #2 is greater than that between vortex #2 and vortex #3. Consequently, vortex #2 and vortex #3 gradually merge and become larger further downstream, resulting in intermittent flameout in the expansion section.

In order to advance the understanding of the underlying mechanisms of flow-induced combustion instability, this work aims to

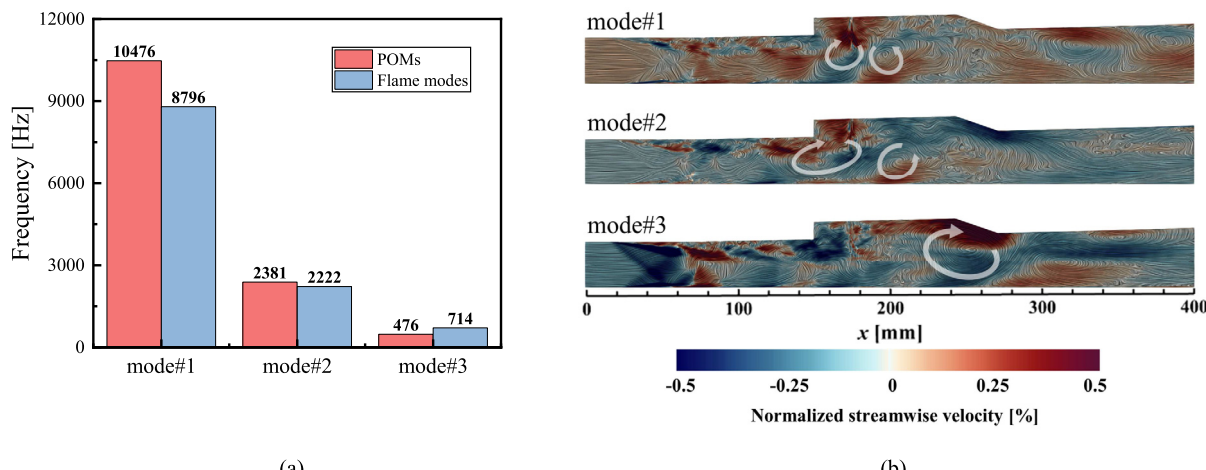


Fig. 15. (a) Temporal comparison of flame modes and POMs. (b) Spatial structures of the first three POMs.

identify large-scale coherent structures that exert a dominant influence on the flow field through the application of Proper Orthogonal Decomposition (POD) [53]. The analysis is conducted on 2-D velocity vector snapshots, and the dominant frequency of each POD mode (POM) is determined through the application of the Fast Fourier Transform (FFT) to their corresponding temporal coefficients. In the snapshot POD approach, the dataset is first arranged into a matrix

$$\psi(x, y, t) = \begin{bmatrix} \mathbf{u}_1(t_1) & \cdots & \mathbf{u}_1(t_N) \\ \vdots & \ddots & \vdots \\ \mathbf{u}_M(t_1) & \cdots & \mathbf{u}_M(t_N) \end{bmatrix} \quad (16)$$

where each column corresponds to a temporal discretization of the whole spatial grid. By calculating the two-point space-correlation tensor in matrix form \mathbf{C} , the eigenvalue λ representing the modal energy and the eigenvector \mathbf{A} are obtained using eigen-decomposition

$$\begin{cases} \mathbf{C} = \psi^T \psi \\ \mathbf{C} \mathbf{A}_i = \lambda_i \mathbf{A}_i \end{cases} \quad (17)$$

Finally, the POMs Φ_i can be obtained by normalizing the basis functions $\mathbf{A}\mathbf{u}$, as well as the temporal coefficients $\mathbf{a}(t)$ are calculated via projecting the raw matrix onto POMs

$$\Phi_i(x, y) = \frac{\sum_{n=1}^N \mathbf{A}_n^i \mathbf{u}_n}{\left\| \sum_{n=1}^N \mathbf{A}_n^i \mathbf{u}_n \right\|} \quad (i = 1, 2, \dots, N) \quad (18)$$

$$\mathbf{a}_i(t) = \Phi_i^T(x, y) \psi(x, y, t) \quad (19)$$

Fig. 15(a) presents a comparison of the frequency between POMs and flame oscillation modes, as discussed previously. It is convincing that the most energetic POM (mode #1) is in close proximity to the dominant flame mode. Similar consistency is also observed in the lower-frequency modes. The spatial structures of the first three POMs are depicted in Fig. 15(b). In mode #1, the rapid exchange of momentum generates a pair of counter-rotating vortices when the high-speed jet penetrates the low-speed separated flow. The upstream vortex, which directly interacts with the fuel jet, explains the periodic variation in the penetration depth of the jet, while the downstream vortex determines the oscillation characteristics of the flame. In mode #2, a similar but larger counter-rotating vortex pair is generated, and the upstream vortex extends to the tail of the isolator. Mode #3 embodies the coherent structures that are related to the largest-amplitude flame oscillation. A single large vortex can be observed at the cavity exit,

which occupies the entire height and entrains the flame into the cavity floor, consistent with the previous analyses. The vortex is generated by the sudden contraction of the channel when entering the expansion section. Therefore, it is expected that low-frequency oscillations of this kind can be suppressed by optimizing the dimensional parameters of the combustor.

4. Concluding remarks

This work performed LES of a hydrogen-fueled direct-injection scramjet using *blastFoam* code combined with detailed finite-rate chemistry. The results satisfactorily reproduced two typical flame structures (cavity shear-layer/cavity assisted jet-wake stabilized flames) corresponding to the scram/ram operating modes, which indicated the solver's capability to effectively model the dual-mode scramjet combustion, as evidenced by the qualitative optical diagnostic images, the quantitative wall pressure measurements and Mach number distributions.

The analyses of the three-dimensional flow characteristics and flame structures have revealed that the discontinuous cavity flame was stabilized by two recirculation zones in scram mode, whereas the jet-wake flame oscillated with the separated flow owing to the lack of the cavity recirculation zone in ram mode. Both modes exhibited a diffusion regime as a whole, with a lean-premixed regime in the narrow layer between the reaction zone and airstream. In scram mode, more than 90% of flow was at supersonic speed and the subsonic recirculation rate reached its peak (1.6%) at the cavity recirculation core. In ram mode, the minimum supersonic flow (43%) was located at the thermal throat, and the recirculation rate in the isolator separation zone (2%) was higher than that in the corner recirculation zone (1.5%).

Scram-to-ram mode transition based on the flame behavior could be divided into three stages. The first one was represented by a swing flame with large-amplitude flame flashback caused by jet/shear-layer interaction. The second one was characterized by the high-frequency flame flashback induced by unsteady heat-release. In the last one, the intensive heat-release promoted the establishment of a large-area separation zone, which led to the oscillation of combustion mode followed by the complete transition. In addition, the unsteady jet-wake ram combustion presented three oscillation modes. The presence of a counter-rotating vortex pair in the front part of the cavity (10476 Hz and 2381 Hz), and a single large-scale vortex at the cavity exit (476 Hz) sustained the large-amplitude shear-layer oscillations, which gave rise to the periodic disintegration of the fuel jet, as well as intermittent flameout further downstream.

Through the comprehensive understanding of flame dynamics attained in the direct-injection dual-mode scramjet, it is imperative to delve into research exploring more practical engine configurations and operational circumstances. Specifically, investigations concerning the application of passive-injection scheme, utilization of ethylene fuel, and the ram-to-scram transition process are essential for future endeavors. Additionally, the implementation of higher grid resolution near the wall and the employment of dynamic turbulent scalar flux model are anticipated to improve the separation capture.

Declaration of competing interest

The authors declare that they have no known competing financial interests or personal relationships that could have appeared to influence the work reported in this paper.

Data availability

No data was used for the research described in the article.

Acknowledgements

The authors thank the support of the Natural Science Foundation of China (NSFC) under Grant No. 91741117, and the High-tech Research Key Laboratory of Zhenjiang (No. SS2018002). The computation work was performed at the HPC Center of Jiangsu University, and *blastFoam* code is open-source by Synthetik Applied Technologies LLC (<https://www.synthetik-technologies.com>).

References

- [1] W. Huang, Z.B. Du, L. Yan, R. Moradi, Flame propagation and stabilization in dual-mode scramjet combustors: a survey, *Prog. Aeronaut. Sci.* 101 (2018) 13–30.
- [2] D. Andreadis, Scramjet engines enabling the seamless integration of air & space operation, *Ind. Phys.* 10 (2004) 24–27.
- [3] F.W. Barnes, C. Segal, Cavity-based flameholding for chemically-reacting supersonic flows, *Prog. Aeronaut. Sci.* 76 (2015) 24–41.
- [4] W. Huang, L. Yan, J.G. Tan, Survey on the mode transition technique in combined cycle propulsion systems, *Aerosp. Sci. Technol.* 39 (2014) 685–691.
- [5] Y. Tian, S. Yang, J. Le, T. Su, M. Yue, F. Zhong, X. Tian, Investigation of combustion and flame stabilization modes in a hydrogen fueled scramjet combustor, *Int. J. Hydrol. Energy* 41 (2016) 19218–19230.
- [6] C. Zhang, J. Chang, J. Ma, W. Bao, D. Yu, J. Tang, Effect of Mach number and equivalence ratio on the pressure rising variation during combustion mode transition in a dual-mode combustor, *Aerosp. Sci. Technol.* 72 (2018) 516–524.
- [7] W. Huang, L. Yan, Numerical investigation on the ram-scram transition mechanism in a strut-based dual-mode scramjet combustor, *Int. J. Hydrol. Energy* 41 (2016) 4799–4807.
- [8] L. Yan, L. Liao, Y.S. Meng, S.B. Li, W. Huang, Investigation on the mode transition of a typical three-dimensional scramjet combustor equipped with a strut, *Energy* 208 (2020) 118419.
- [9] H. Wang, Z. Wang, M. Sun, H. Wu, Combustion modes of hydrogen jet combustion in a cavity-based supersonic combustor, *Int. J. Hydrol. Energy* 38 (2013) 12078–12089.
- [10] Y. Yuan, T. Zhang, W. Yao, X. Fan, P. Zhang, Characterization of flame stabilization modes in an ethylene-fueled supersonic combustor using time-resolved CH* chemiluminescence, *Proc. Combust. Inst.* 36 (2017) 2919–2925.
- [11] D. Cao, H.E. Brod, N. Yokey, D. Michaels, Flame stabilization and local combustion modes in a cavity-based scramjet using different fuel injection schemes, *Combust. Flame* 233 (2021) 111562.
- [12] Z. Du, C. Shen, W. Huang, Y. Han, Investigation on the impact of the induced shock wave on the hydrogen mixing augmentation in a supersonic crossflow: a numerical study, *Fuel* 312 (2022) 122961.
- [13] S.A. Mecklem, W.O. Landsberg, D. Curran, A. Veeraragavan, Combustion enhancement via tandem cavities within a Mach 8 scramjet combustor, *Aerosp. Sci. Technol.* 124 (2022) 107551.
- [14] X. Zhong, W. Huang, L. Yan, H. Wu, Z. Du, Investigation on the adaptive control of shock wave/turbulent boundary layer interaction based on the secondary circulation jets, *Acta Astronaut.* 198 (2022) 233–250.
- [15] E. Hassan, T.M. Ombrello, D.M. Peterson, Computational and experimental investigation of ignition in a Mach 2 cavity-based flameholder, *Aerosp. Sci. Technol.* 115 (2021) 106756.
- [16] H. Ouyang, W. Liu, M. Sun, The large-amplitude combustion oscillation in a single-side expansion scramjet combustor, *Acta Astronaut.* 117 (2015) 90–98.
- [17] G. Zhao, M. Sun, J. Wu, X. Cui, H. Wang, Investigation of flame flashback phenomenon in a supersonic crossflow with ethylene injection upstream of cavity flameholder, *Aerosp. Sci. Technol.* 87 (2019) 190–206.
- [18] M.L. Fotia, J.F. Driscoll, Ram-scram transition and flame/shock-train interactions in a model scramjet experiment, *J. Propuls. Power* 29 (2013) 261–273.
- [19] H. Wang, Z. Wang, M. Sun, N. Qin, Large-Eddy/Reynolds-averaged Navier-Stokes simulation of combustion oscillations in a cavity-based supersonic combustor, *Int. J. Hydrol. Energy* 38 (2013) 5918–5927.
- [20] S. Nakaya, H. Yamana, M. Tsue, Experimental investigation of ethylene/air combustion instability in a model scramjet combustor using image-based methods, *Proc. Combust. Inst.* 38 (2021) 3869–3880.
- [21] Q. Liu, D. Baccarella, T. Lee, Review of combustion stabilization for hypersonic airbreathing propulsion, *Prog. Aeronaut. Sci.* 119 (2020) 100636.
- [22] H. Sitaraman, S. Yellapantula, M.T.H. de Frahan, B. Perry, J. Rood, R. Grout, M. Day, Adaptive mesh based combustion simulations of direct fuel injection effects in a supersonic cavity flameholder, *Combust. Flame* 232 (2021) 111531.
- [23] N.T. Clemens, V. Narayanaswamy, Low-frequency unsteadiness of shock wave/turbulent boundary layer interactions, *Annu. Rev. Fluid Mech.* 46 (2014) 469–492.
- [24] S.J. Laurence, D. Lieber, J.M. Schramm, K. Hannemann, J. Larsson, Incipient thermal choking and stable shock-train formation in the heat-release region of a scramjet combustor. Part I: shock-tunnel experiments, *Combust. Flame* 162 (2015) 921–931.
- [25] J. Zhang, J. Chang, C. Kong, H. Qiu, W. Bao, Flame oscillation characteristics in a kerosene fueled dual mode combustor equipped with thin strut flameholder, *Acta Astronaut.* 161 (2019) 222–233.
- [26] Z. Wang, J. Chang, G. Wu, D. Yu, Experimental investigation of shock train behavior in a supersonic isolator, *Phys. Fluids* 33 (2021) 046103.
- [27] Q. Yang, J. Chang, W. Bao, J. Deng, A mechanism of combustion mode transition for hydrogen fueled scramjet, *Int. J. Hydrol. Energy* 39 (2014) 9791–9797.
- [28] N. Kato, S. Im, Flame dynamics under various backpressures in a model scramjet with and without a cavity flameholder, *Proc. Combust. Inst.* (2020) 3861–3868.
- [29] C. Aguilera, K.H. Yu, Scramjet to ramjet transition in a dual-mode combustor with fin-guided injection, *Proc. Combust. Inst.* 36 (2017) 2911–2918.
- [30] M.B. Sun, Z. Cai, Y. Wang, G. Zhao, Y. Sun, P. Li, M. Wan, L. Li, Overview on the research progress of unsteady supersonic combustion, *Acta Aerodyn. Sin.* 38 (2019) 532–551.
- [31] P. Wang, S.M. Hashemi, H. He, K. Cheng, Investigation of the partially premixed turbulent combustion through the PRECCINSTA burner by large eddy simulation, *Aerosp. Sci. Technol.* 121 (2022) 107336.
- [32] M. Yuan, P. Wang, Y. Zhang, A. Ferrante, Large eddy simulation of flame and thermal-acoustic characteristics in a strut-based scramjet with dynamic thickened flame model, *Case Stud. Therm. Eng.* 41 (2023) 102560.
- [33] P.J. Vonk, M. Safdari, M.D. Brandyberry, A new OpenFOAM solver for compressible multi-fluid flow with application to high-explosive detonation, in: 4th OpenFOAM User Conference, Cologne, 2016.
- [34] B.J. McBride, Coefficients for Calculating Thermodynamic and Transport Properties of Individual Species, NASA Langley Research Center, 1993.
- [35] A. Yoshizawa, K. Horiuti, A statistically-derived subgrid-scale kinetic energy model for the large-eddy simulation of turbulent flows, *J. Phys. Soc. Jpn.* 54 (1985) 2834–2839.
- [36] W.W. Kim, S. Menon, A new dynamic one-equation subgrid-scale model for large eddy simulations, in: 33rd Aerosp. Sci. Meet. & Exhib.Reno, 1995, p. 356.
- [37] A. Karlsson, Modeling Auto-Ignition, Flame Propagation and Combustion in Non-Stationary Turbulent Sprays, 1995.
- [38] N. Marinov, C. Westbrook, W. Pitz, Detailed and global chemical kinetics model for hydrogen, *Transp. Phenom. Combust.* 1 (1996) 118–129.
- [39] Z. Huang, G. He, F. Qin, X. Wei, Large eddy simulation of flame structure and combustion mode in a hydrogen fueled supersonic combustor, *Int. J. Hydrol. Energy* 40 (2015) 9815–9824.
- [40] Z. Huang, G. He, S. Wang, F. Qin, X. Wei, L. Shi, Simulations of combustion oscillation and flame dynamics in a strut-based supersonic combustor, *Int. J. Hydrol. Energy* 42 (2017) 8278–8287.
- [41] N. Nordin, Detailed chemistry spray combustion model for the KIVA code, in: User's Group Meeting at the SAE Congress, 2001.
- [42] R.J. Spiteri, S.J. Ruuth, A new class of optimal high-order strong-stability-preserving time discretization methods, *SIAM J. Numer. Anal.* 40 (2002) 469–491.
- [43] W. Xie, R. Zhang, J. Lai, H. Li, An accurate and robust HLLC-type Riemann solver for the compressible Euler system at various Mach numbers, *Int. J. Numer. Methods Fluids* 89 (2019) 430–463.
- [44] G. Wanner, E. Hairer, Solving Ordinary Differential Equations II, Springer Berlin Heidelberg, New York, 1996.
- [45] P. Xiong, D. Zheng, Y. Tan, Y. Tian, J. Le, Experimental study of ignition and combustion characteristics of ethylene in cavity-based supersonic combustor at low stagnation temperature and pressure, *Aerosp. Sci. Technol.* 109 (2021) 106414.

- [46] Y. Tian, S. Yang, J. Le, F. Zhong, X. Tian, Investigation of the effects of fuel injector locations on ignition and flame stabilization in a kerosene fueled scramjet combustor, *Aerosp. Sci. Technol.* 70 (2017) 310–316.
- [47] T.S. Lund, X. Wu, K.D. Squires, Generation of turbulent inflow data for spatially-developing boundary layer simulations, *J. Comput. Phys.* 140 (1998) 233–258.
- [48] E.R. Van Driest, Turbulent boundary layer in compressible fluids, *J. Aeronaut. Sci.* 18 (1951) 145–160.
- [49] N. Hass, K. Cabell, A. Storch, M. Gruber, HIFiRE direct-connect rig (HDCR) phase I scramjet test results from the NASA Langley arc-heated scramjet test facility, in: 17th AIAA International Space Planes and Hypersonic Systems and Technologies Conference, 2011, p. 2248.
- [50] W.H. Heiser, D.T. Pratt, D.H. Daley, *Hypersonic Airbreathing Propulsion*, AIAA, 1994.
- [51] R. Bilger, S. Stärner, R. Kee, On reduced mechanisms for methane-air combustion in nonpremixed flames, *Combust. Flame* 80 (1990) 135–149.
- [52] C. Liu, Y. Zhao, Z. Wang, H. Wang, M. Sun, Dynamics and mixing mechanism of transverse jet injection into a supersonic combustor with cavity flameholder, *Acta Astronaut.* 136 (2017) 90–100.
- [53] L. Sirovich, Turbulence and the dynamics of coherent structures. I. Coherent structures, *Q. Appl. Math.* 45 (1987) 561–571.